Física de la Tierra
2000, 12, 105-126

ISSN: 0214-4557

Radio Sounding of Geospace Plasmas

B. W. REINISCH
University of Massachusetts, Lowell
Environmental, Earth, and Atmospheric Sciences Department
Center for Atmospheric Research
Lowell, MA, USA

ABSTRACT

New techniques for the radio sounding of geospace plasmas are described. Advanced digital processing, including spread-spectrum and Fourier techniques, has been successfully deployed during the last decade. Similar techniques have recently been applied to space-borne sounding of the magnetosphere. It is shown that radio sounding using Doppler-sorted imaging can measure the structure and dynamics of geospace plasmas.

Key words: Radio Sounding Geospace Plasmas, Doppler-Sorted Imaging.

1. INTRODUCTION

Radio sounding is a well-established technique that was first deployed in the 1920's for ionospheric sounding from the ground (Breit and Tuve, 1926). In recent years, advanced digital sounders were developed for ground-based observations that provide detailed information about the structure and dynamics of the bottomside ionosphere (Reinisch, 1996). These modern sounders measure more than just the time of flight and amplitude of the echoes, they also determine the arrival angle, wave polarization, and Doppler frequency. Radio sounding relies on total reflection of radio waves from plasma structures that have plasma frequencies f_N equal to the radio frequencies f. It is, therefore, not possible on the ground to receive echoes reflected from the topside ionosphere or the magnetosphere since the ionospheric F2 layer prevents all transmitted waves with frequencies $f <$ foF2 (the maximum ionospheric plasma frequency) from propagating beyond the height of the F2 layer peak. The electron density distribution above the F2 peak was measured by topside ionospheric sounders on satellites above the F2 layer peak as first described by Franklin and Maclean (1969). These topside sounders recorded the amplitudes and echo delay times of ionospheric echoes as a function of frequency in the

same way as it was done by the ground-based sounders of the time. Data from the highly successful Alouette/ISIS topside sounders (Jackson et al., 1980; Jackson, 1986) were the basis for nearly 1,000 scientific publications (Benson et al., 1998; Pulinets, 1989). Very recently, radio sounding techniques for magnetospheric sounding were developed using frequencies from 3 kHz to 3 MHz (Reinisch et al., 2000), corresponding to electron densities $N_e \approx 10^5$ to 10^{11} m^{-3}.

2. PRINCIPLES OF RADIO SOUNDING

Remote sensing of space plasmas with radio waves was originally developed for ground-based ionospheric observations using different techniques: partial reflection (2-6 MHz), total reflection or radio sounding (0.1 –30 MHz), coherent scatter (10-100 MHz), and incoherent scatter (50-900 MHz) (Hunsucker, 1992). Electromagnetic waves can propagate through a magnetoionic medium as long as $n^2 > 0$ where n is the index of refraction. Reflection occurs where $n = 0$ and the plasma density gradient is parallel to the wave normal (Budden, 1985). Solving Maxwell's equation for $n = 0$ gives the following three reflection conditions:

$X = 1$ ordinary (O) wave mode
$X = 1 - Y$ extraordinary (X) wave mode
$X = 1 + Y$ Z-wave mode (1)

$$X = \left(\frac{f_N}{f}\right)^2, Y = \frac{f_H}{f}, f_N = \sqrt{\frac{N e^2}{4\pi^2 m \varepsilon_0}}, f_H = \frac{eB_0}{2\pi m}.$$

N, e, and m are the number density, charge, and mass of the electron, ε_0 is the free space permittivity, and B_0 is the earth's magnetic field. The O and Z modes have left-hand, and the X mode right-hand polarization with respect to the magnetic field direction. Except at high latitudes, the Z mode is rarely observed and the two prevailing modes, O and X, can be identified by the sense of rotation of the **E** field vector. Ionosondes typically scan through frequencies from ~0.5 to 30 MHz transmitting narrow pulses in the vertical direction and measuring the echo delay time. The data can be displayed in form of an ionogram showing the echo delay as function of the sounding frequency. The echo delay t_d is usually expressed in terms of the virtual height $h' = 0.5\ c\ t_d$ where c is the free space speed of light. The quiet daytime ionogram in Figure 1 was recorded at Millstone Hill, Massachusetts (42(N) and shows echoes from the E, F1 and F2 layers. This ionogram is easy to interpret since the ionosphere showed no irregularities and all the echoes were returned from directly overhead.

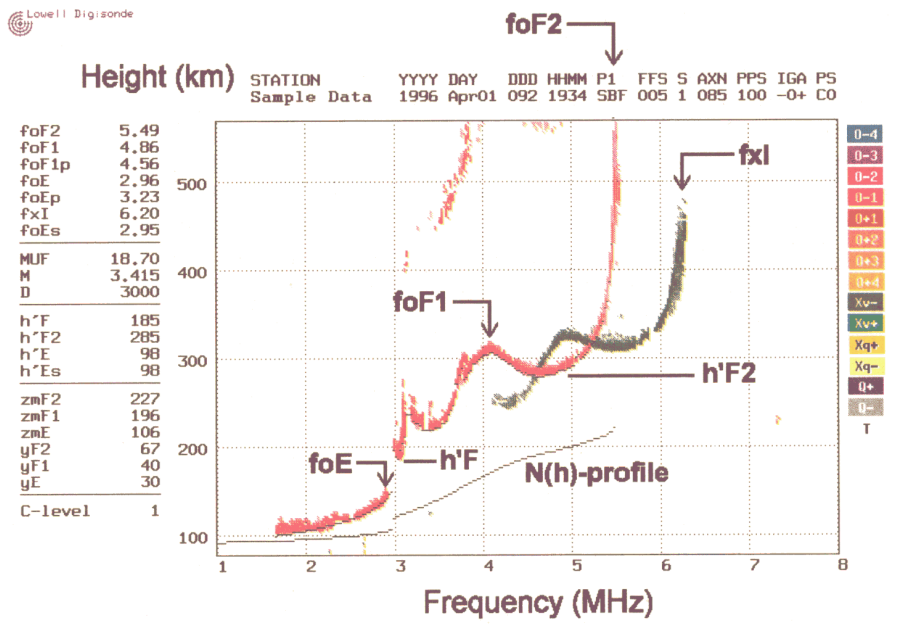

Figure 1. Quiet daytime ionogram at Millstone Hill. The *O* and *X* echo traces are identified by red and green color. The autoscaled $h'(f)$ traces are shown as thin black lines close to the leading edge of the echo traces. Some of the autoscaled ionogram characteristics are displayed on the left. The automatically calculated electron density profile is shown in the ionogram as an $f_N(f)$ plot.

3. THE WAVE POLARIZATION

Electromagnetic wave propagation in a magnetoionic medium is anisotropic, and only waves with the characteristic wave polarizations are solutions of Maxwell's equations (Stix, 1962; Budden, 1985). The two characteristic polarizations are generally right- and left-hand elliptical, and the two characteristic waves propagate with different phase and group velocities. The modes have different plasma cutoff frequencies as discussed above, corresponding to different reflection levels and echo delays. Since the plasma is generally not homogeneous, the characteristic polarizations slowly change along the ray path. Significant mode conversion does not occur unless steep gradients are encountered. When receiving echoes on the ground, the characteristic polarizations are determined at the altitude where the signal exits the ionosphere (Budden, 1985). For topside or magnetospheric space-based sounding, the characteristic polarizations of the received echo signals are defined by the local plasma frequency f_{NS} and the magnetic field $\mathbf{B}_{0S}$ at the spacecraft location. Except for nearly transverse propagation with respect to the geomagnetic field direction, the

elliptical polarizations are almost circular, i.e., the ratio ρ of the minor axis over the major axis of the polarization ellipse is ≥ 0.9. Modern sounders make use of that fact and transmit right-or left-hand polarized waves thus putting nearly 100% of the radiated energy into the desired wave mode. If the receive antennas are also circular polarized, it is easy to distinguish the *O* and the *X* mode echoes by transmitting/receiving successively with *O* and *X* antenna polarization. A simple right- or left-hand polarized antenna can be built with two linear orthogonal antennas by feeding two equal currents with phase difference $\Delta\phi$ into the two antennas for transmission, or by adding the two signal with a phase delay of $-\Delta\phi$ for reception. In most applications, $\Delta\phi = 90°$ (Reinisch et al., 1997), and the transmitted signal at a point r, θ, ϕ becomes (Reinisch et al., 1999)

$$\mathbf{E}(t, r, \theta, \phi) = (E_x\hat{\mathbf{x}}, E_y\hat{\mathbf{y}}, E_z\hat{\mathbf{z}})\, e^{i(\omega t - kr)} \tag{2a}$$

with

$$\begin{aligned} E_x &= E_0\,[(1 - \sin^2\theta\cos^2\phi) \mp i(\sin^2\theta\cos\phi\sin\phi\sin\phi)] \\ E_y &= E_0\,[-\sin^2\theta\cos\phi\sin\phi \pm i(1 - \sin^2\phi\sin\phi\sin^2\phi)] \\ E_z &= E_0\,[-\sin\theta\cos\theta\cos\phi \mp i(\sin\theta\cos\theta\sin\phi)] \end{aligned} \tag{2b}$$

The two orthogonal antennas (dipoles, rhombics, or deltas) are assumed to line up with the x and y axes, and the currents into the antennas are $I_y(t) = \pm i\, I_x(t)$. The plus-or-minus sign determines the sense of rotation; for the upper signs, **E** rotates from the x to the y axis. In ionospheric sounding the characteristic waves are generally called *X* and *O* waves, plasma wave studies prefer the designations *R*-*X* and *L*-*O* waves, meaning right and left hand polarized with respect to the direction of the magnetic field or its component in the direction of propagation. Since the **E** vector of an *R* wave (*L* wave) rotates in the same direction as a gyrating electron (positive ion), Rawer and Suchy (1967) suggested the designations e-wave and i-wave. These two waves are shown in Figure 2 for $\theta < 90°$ and $\psi < 90°$. The wave polarization is circular for $\theta = 0°$ and 180°, linear for $\theta = 90°$ and elliptical for all other directions.

4. CONCEPTS OF MODERN PLASMA SOUNDERS

Modern sounders measure all parameters of the waves reflected from multiple plasma structures: the echo delay time, the complex spectrum (amplitude and phase) of the echo signals, their arrival angle, and their wave polarization. In contrast to conventional radar systems, sounders operate over a large frequency range requiring wideband antenna systems. The long wavelengths involved in the sounding of geospace plasmas make it impractical to construct narrow-beam transmit antennas. The beam width of typical transmit antennas used for radio sounding is usually large, $\sim\pi/2$ radian for ground-based ionospheric

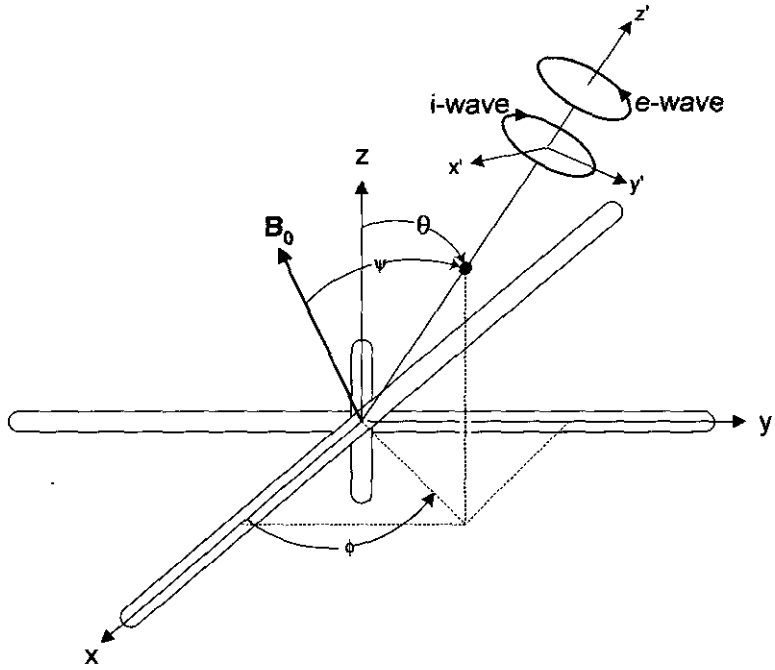

Figure 2. Transmission into direction z' from orthogonal antennas along the x and y axes. The senses of rotation for the i and e waves are shown for $\psi < 90^{o}$.

sounding, and 4π steradian for space-based sounding. This means that a large region of plasma-filled space is illuminated. Depending on the plasma structure, echoes can return from many directions. This creates complicated ionogram images (unlike Figure 1) with overlapping vertical and oblique *O* and *X* echoes. To correctly identify and interpret these echoes in terms of plasma density and echolocation it is necessary, therefore, to measure the wave polarization and the arrival angle of the echoes. Measuring the Doppler shifts of the individual echoes allows the deduction of the velocity vector of the moving plasma, making it often possible to derive the plasma drift from Doppler-interferometric soundings. Indeed, Doppler analysis, i.e., Fourier transformation, of the received echo signals is the only way to identify the multiple signals arriving simultaneously at the receiver from different directions. The spaced-antenna interferometer technique, usually deployed for arrival angle measurements on the ground, can give the arrival angle only when a single plane wave is arriving. The arrival angle can then simply be calculated from the signal phases measured on three or more spaced antennas. The same condition applies for the single point spacecraft technique. The condition of a single plane wave is normally not satisfied since echoes from different directions will superimpose. For pulsed

signals, only echoes from targets with a virtual distance between R' and $R' + c \cdot PW/2$ will superimpose where PW the pulse width. The virtual target distance, i.e., the radar range R', is equal to the virtual height h' for ground-based vertical ionospheric sounding. Measuring the phases of the composite signal does not allow one to determine the echo arrival angles. Bibl and Reinisch (1978) overcame this difficulty by first Fourier analyzing the echo signals, thus separating any time-coincident echoes by making use of the direction-dependent Doppler shifts. Most ground-based modern sounder installations have four, some seven, receive antennas and their spacing is typically in the order of a wavelength or less. The Doppler shift d_j of echo j is given by (Reinisch et al., 1987)

$$d_j = \frac{1}{\pi} \mathbf{k}_j \cdot \mathbf{v} \tag{3}$$

where $\mathbf{k}_j = \frac{2\pi}{\lambda} \hat{\mathbf{k}}_j$ is the wave vector of echo j, and $\hat{\mathbf{k}}_j$ the corresponding unit vector; $\mathbf{v}$ is the velocity of the reflecting plasma. As long as the plasma velocity $v \neq 0$, echoes from different directions have generally different Doppler frequencies depending on the angle between $\mathbf{k}_j$ and $\mathbf{v}$, and therefore each reflection point, or source j, has its own component in the Fourier spectrum. Applying interferometry to each spectral component d_j of the signal can determine the arrival angles for the different echoes. For space-borne single satellite observations where the antenna spacing required for interferometry is not available, a different technique using three orthogonal antennas is applied to find the angle of arrival as discussed below.

5. ADVANCED SOUNDERS FOR GROUND-BASED IONOSPHERIC OBSERVATIONS

Recent progress in digital technology has made it possible to implement the measuring capabilities for the different parameters discussed above into instruments of small size, low radiated power, and moderate costs. Automatic scaling of the ionograms in real time and automated calculation of the electron density profile is nowadays widely available. The University of Massachusetts Lowell developed «Digisondes» are likely the best example of an advanced ionosonde, with some 70 Digisondes currently operating worldwide. We will therefore describe the Digisonde Portable Sounder (DPS) as an example of a modern sounder. Other digital sounders with scientific capabilities that are currently in use include the CADI (McDougal et al., 1995) the AIS (Grubb, 1979), the Dynasonde (Wright and Pitteway, 1979), and the PARUS (Reznikov, 1991). The chirp sounder (Barry, 1971), which linearly changes frequency with time, has not found wide scientific applications.

The system diagram for the DPS (Reinisch, 1996) in Figure 3 indicates the two orthogonal transmit antennas and the four polarized receive antennas (Figure 4). Each receive antenna consists of two crossed loops, and the two an-

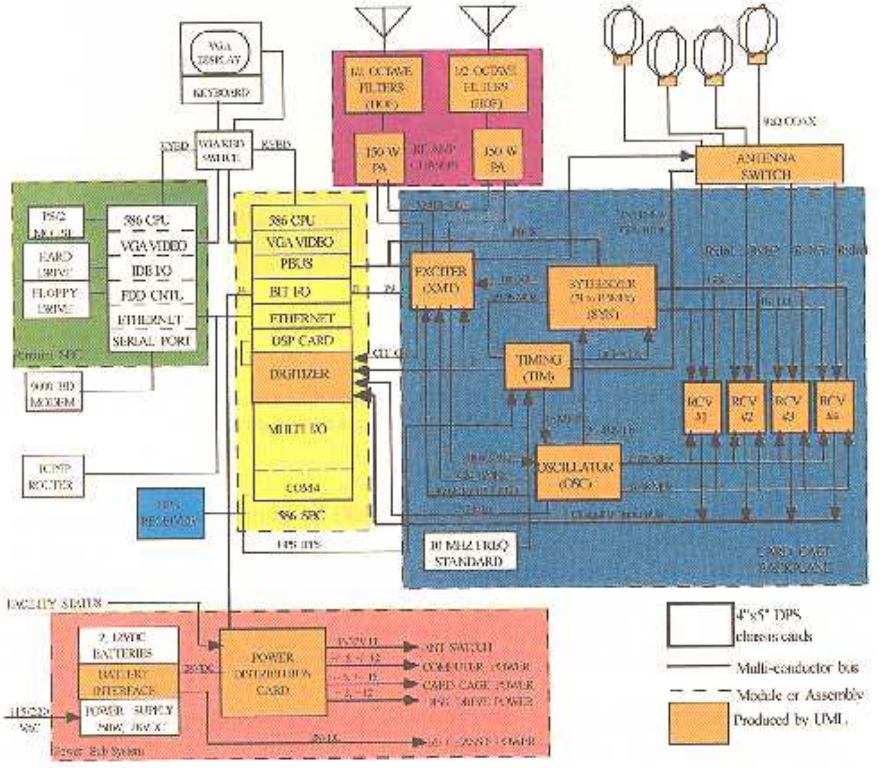

Figure 3. DPS Block diagram.

tenna signals are added or subtracted in a 90° hybrid. By changing the polarization of the transmitting and receiving antennas from pulse to pulse, the system is able to automatically identify the ordinary and extraordinary wave polarizations, as illustrated in Figure 1. Table 1 illustrates the performance characteristics of a modern ionosonde, using the DPS as an example. As shown, the transmitter power is only a few hundred watts as compared to the ~10 kW used in earlier sounders, including the Digisonde 256 (Reinisch et al., 1989). This became possible when Haines (1994) introduced the spread spectrum techniques to ionospheric sounding. By spreading the transmitted energy over eight 66-ms phase-coded pulses, forming the 533 ms transmitter pulse, and

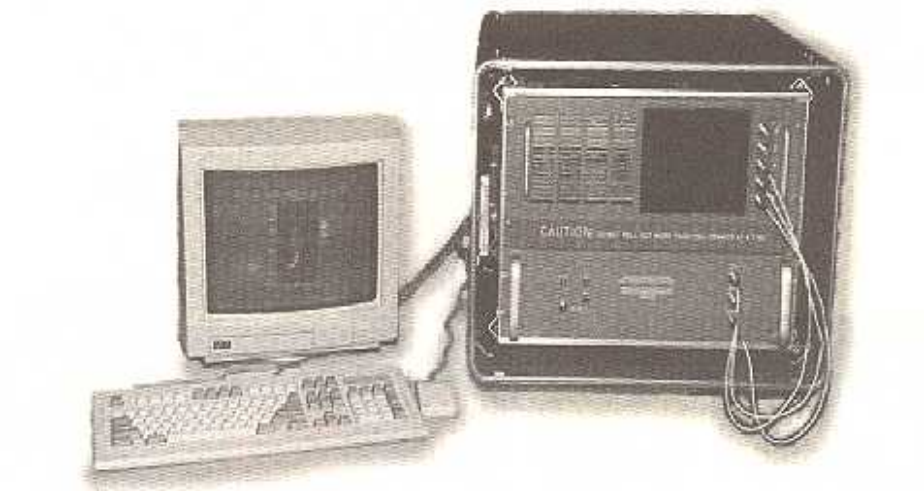

Figure 4. Example of a modern ionosonde, the DPS (4a), with the crossed-loop receive antenna (4b) and the configuration of the four-antenna receive array (4c).

using complimentary coded pairs makes the 300 W transmission equivalent to a 5 kW uncoded pulse. Using complimentary phase coding in two consecutive pulses leads to clean pulse compression with range leakages that are ~40 dB below the signal peak (Haines, 1994). Coherent spectral integration, i.e., Fourier transformation, over typically 64 pulse pairs produces a digital processing gain of 18 dB, increasing the equivalent transmit power by another 18 dB to ~300 kW.

The Fourier transformation decomposes the received signal into the component signals arriving from the diverse reflection points (sources). The location of each source can then be calculated from the spectral phases obtained for the four antenna signals. The resulting «skymaps» reveal the structure of the reflecting plasma. The sequence of skymaps in Figure 5 was recorded near the Appleton anomaly in Chile (Sales et al., 1996). The measured Doppler frequency of each source is proportional to the source's line-of-sight (LOS) velocity, and one can therefore calculate the velocity vector of the moving irregularities from the ensemble of LOS velocities. This technique is routinely used to measure ionospheric drifts at high latitudes (Reinisch et al., 1987; Cannon et al., 1991; Scali et al., 1995; Smith et al., 1998).

To make the complicated ionosonde data user-friendlier, considerable efforts were made to automatically evaluate them in terms of the vertical electron density profiles and ionospheric characteristics. The Digisondes use the ARTIST software package for the online scaling and profile calculation (Reinisch and Huang, 1983). Real time data, including ionograms, profiles, and

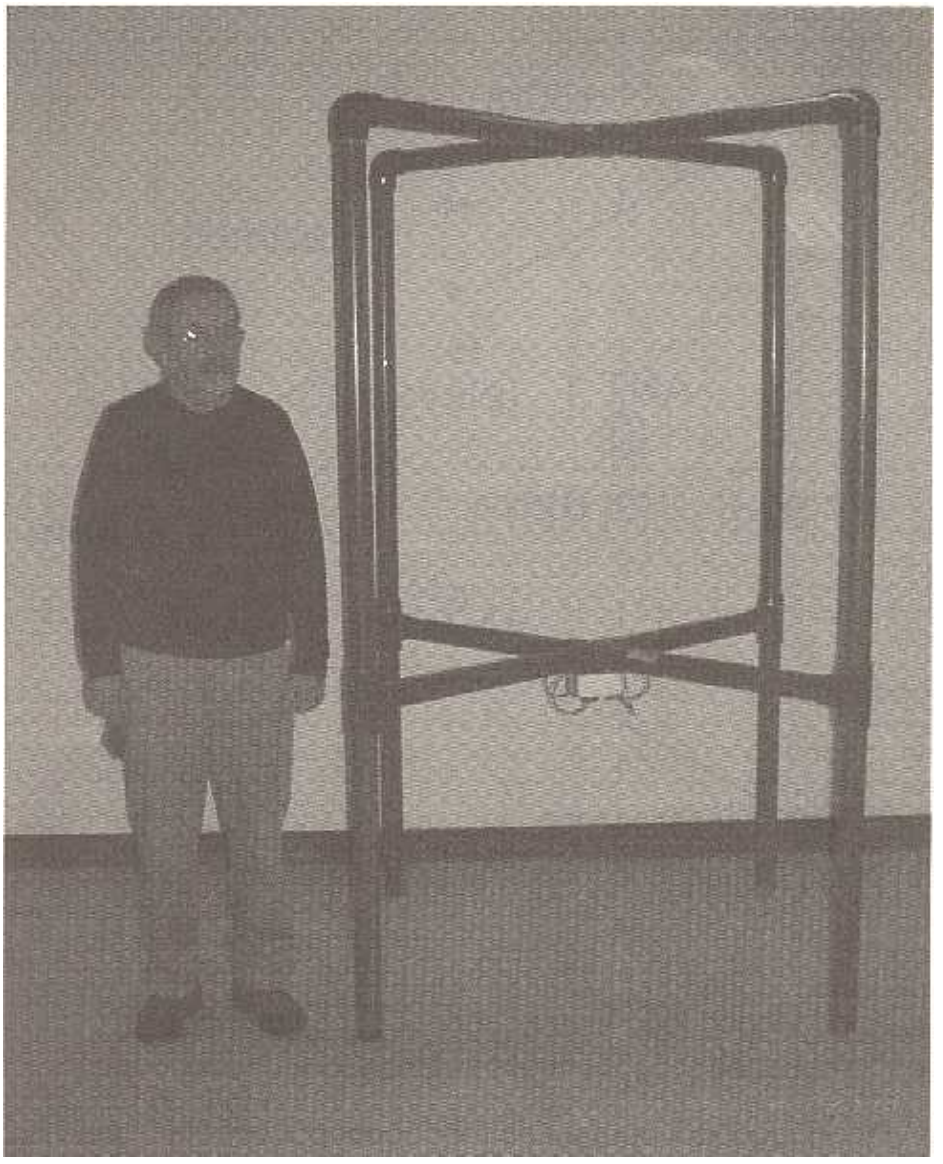

Figure 4b.

ionospheric characteristics can be found on the web (http://ulcar.uml.edu/stationlst/) for many Digisonde stations. GIF files, like the example in Figure 1, give a quick-look of the data.

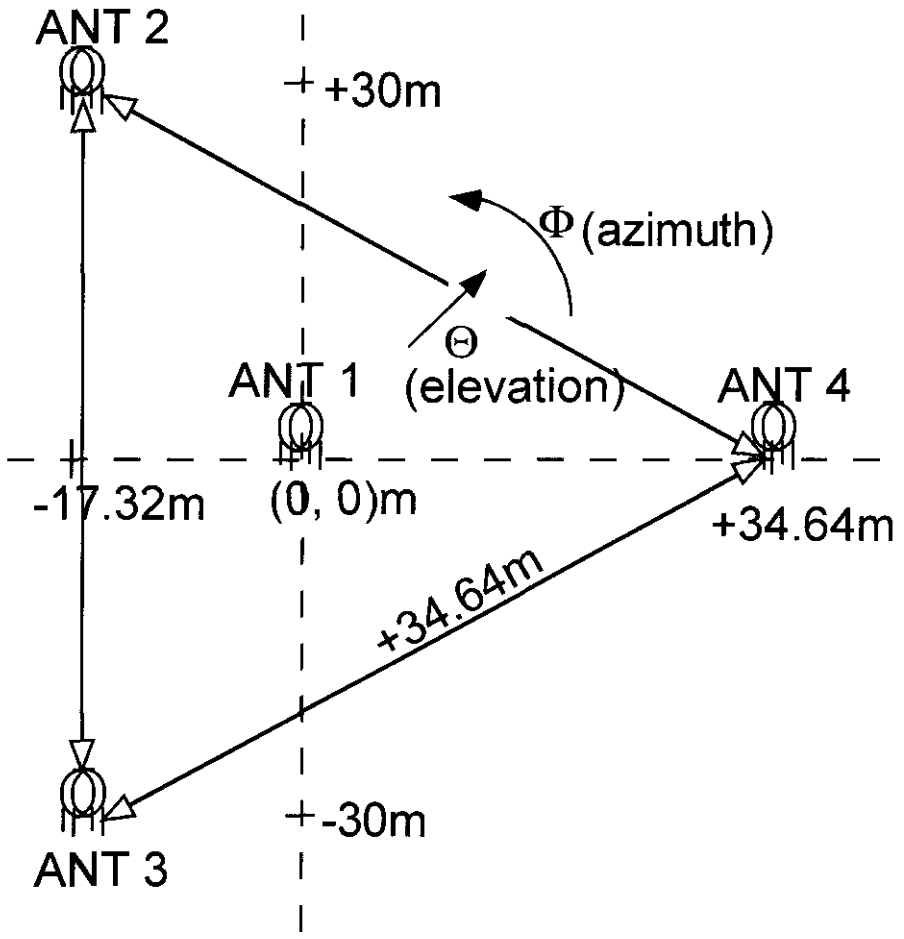

Figure 4c.

6. ADVANCED SPACE-BORNE SOUNDERS

The advanced techniques described in «Advanced Sounders for Ground-Based Ionospheric Observations» for ground-based sounders have recently been implemented into space instrumentation. In March 2000, NASA's IMAGE satellite (Burch, 2000) was launched into a polar elliptical orbit carrying the first advanced plasma sounder into space, the Radio Plasma Imager (RPI) (Reinisch et al., 2000). Designed for sounding in the magnetosphere, RPI operates at frequencies between 3 kHz and 3 MHz covering plasma densities from 10^5 to 10^{11} m^{-3}. RPI has three orthogonal antennas: two 500-m long dipole an-

Table I. Performance specifications of a modern ionosonde system, the DPS

DPS-1 General Specifications (for all operating modes and configurations)

RECEIVER	
Frequency Range	1.0-40 MHz (all modes of operation)
Bandwidth	17 kHz @ 6 dB (for 10 km pulse resolution)
Input Impedance	50 Ω
Noise Figure	11 dB (at receiver antenna preamplifier)
Receiver Sensitivity	–126 dBm into main chassis. Sensitivity is greater at preamplifier (amount depending on gain setting)
Spurious Free Dynamic Range	>80 dB instantaneous >120 dB total operating range including gain control
3rd Order Intercept	>26 dBm (unaffected by –100 dB inband/out of band ratio)
2nd Order Intercept	>30 dBm
Output	12-bit quadrature samples (16-bit after pulse compression)
RF Transmitter	
Frequency Sweep	1-40 MHz, Start, stop and step size settable to 1 kHz
Ionogram Sweep Time	Standard VIS ionogram 200 sec (varies with programmable settings)
Frequency Synthesis	Fully digital (frequency switching time < 1 μs)
Pulse Repetition Rate	50, 100 and 200 pps
Pulse Width	33 to 533 μs for VIS waveform, 275 ms for OIS
Peak Pulse Power	300 W or 150 W (same in any operating mode)
Output Impedance	50 Ω
Transmitter Type	Dual RF MOSFET Amplifiers (second Amp for polarized transmission or serves as «hot» spare)
Lightning Protection	Metal Oxide Varistor and in-line gas discharge devices
User Interface	
Unattended operation	Controlled by 7 programs, 6 schedules & 1 schedule table
Remote access & control (by Internet or modem)	Input/Output access to schedules, measurement data, or diagnostic data, and operating software
Time Setting	Integrated GPS receiver keeps time to +/-25 ms
Built-in Self Test (BIT)	Full diagnostics to isolate failures to replaceable units run automatically and provide remotely accessible data
Self Calibration	Built-in internal cal automatically updates phase/ amplitude adjustment tables. Remotely accessible results.
Signal Processing	
Processors	Two Industrial x586's and Texas Instruments TMS320C40
Range Bins	Up to 512
Height Range	0-2560 km (0 km used for self-calibration)
Height Resolution	10 km (reciprocal of receiver bandwidth) 250 m using High Range Resolution measurement
Amplitude Resolution	3/8 dB
Wave Polarization	O, X or linear (switching NS and EW): Automatically synchronized transmitter and receiver antenna polarization doubles reliability of O/X identification

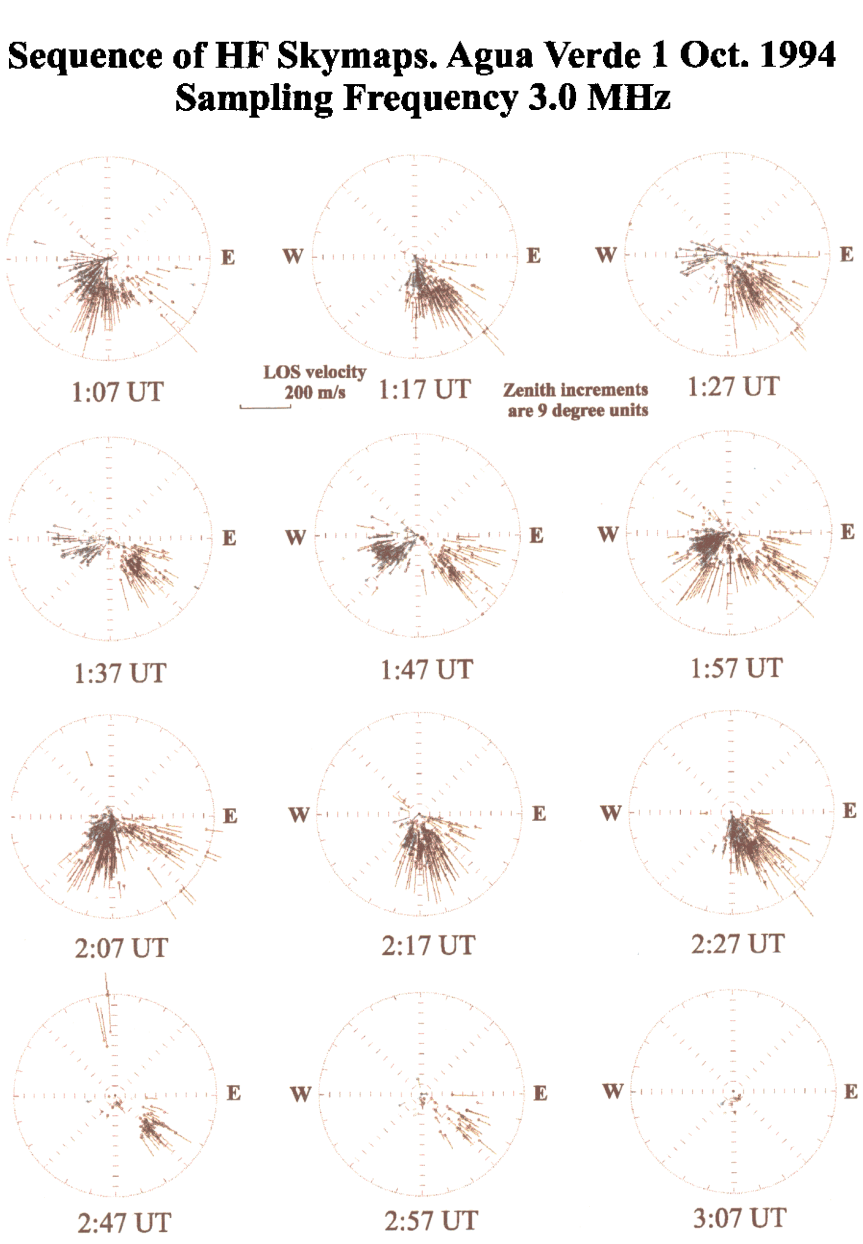

Figure 5. 10-min sequence of skymaps at Agua Verde, Chile, on 1 October 1994. The tick marks indicate 9º increments in zenith angle. Each skymap represents a 20 s observation. The approaching sources with positive Doppler shift are shown in blue, the receding sources in brown.

tennas in the spin plane and a 20-m dipole along the spin axis. Echoes from the magnetopause, plasmasphere and cusp can be received with the three orthogonal antennas, allowing the determination of their angle-of-arrival as described below. The long wire antennas are used for transmission; tuning of the transmit antennas provides optimum power transfer from the 10 W transmitter to the antennas. The instrument can operate in three active sounding modes: (1) remote sounding to probe magnetospheric boundaries, (2) local (relaxation) sounding to probe the local plasma frequency and scalar magnetic field, and (3) whistler stimulation sounding. In addition, there is a passive mode to record natural emissions, and to determine the local electron density, the scalar magnetic field, and temperature by using a thermal noise spectroscopy technique (Meyer-Vernet and Perche, 1989). Unlike the passive plasma wave instruments on other satellites, e.g., WIND (Bougeret et al., 1995) and POLAR (Gurnett et al., 1995), RPI uses the *active* Doppler radar techniques for the remote sensing of plasma structures.

The highly eccentric IMAGE orbit (Figure 6) positions the spacecraft for many hours near its apogee at a geocentric distance of 8 R_E. In the magnetospheric cavity, N_e is generally less than $10^6\,m^{-3}$, which means that the local plasma frequency f_N is less than 9 kHz. Electromagnetic waves with frequencies $f > f_N$ will propagate away from the spacecraft almost as in free space. Depending

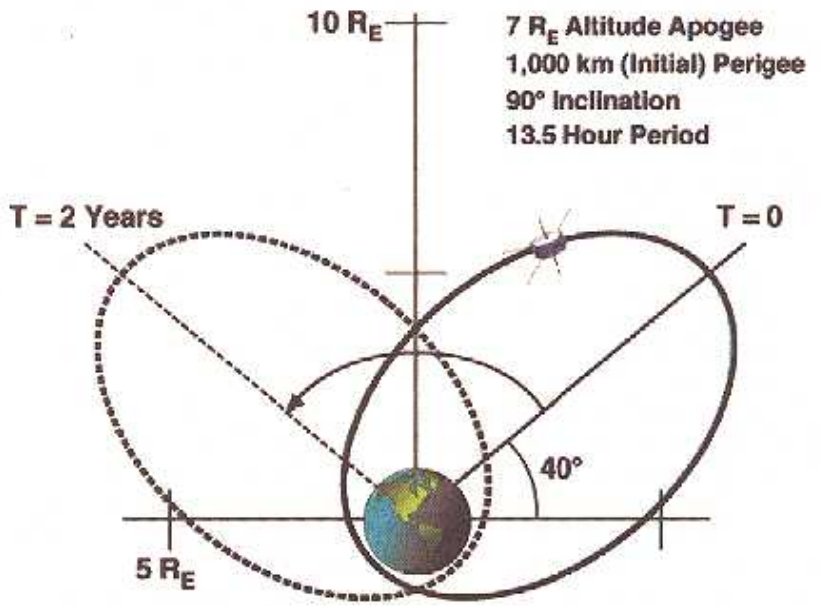

Figure 6. The IMAGE orbit.

on the geometry of the magnetospheric boundaries with respect to the spacecraft location, RPI can «see» several plasma structures simultaneously out to ranges of several R_E. The scientific objectives for the RPI observations include the detection of plasma influx into the magnetosphere during magnetic substorms and storms, and the assessment of the response of the magnetopause and plasmasphere to variations of the solar wind (Fusilier et al., 2000). Figure 7 shows the RPI system diagram. The 10 W RF amplifiers, the CPU switched antenna-matching circuits (couplers), and the receiver preamplifiers are mounted at the foot of each of the *X* and Y long-wire antennas. The two preamplifiers for the *Z* antennas are mounted in a common box at the *Z* antenna feed. The VME chassis for the RPI electronics contains two transmitter exciters, three receivers, the synthesizer, digitizer, and the digital control and power circuits. The power amplifier and coupler for one antenna element is shown in Figures 8a and b. To minimize interference in other instruments on the spacecraft, the radiated power is limited to 10 W by controlling the output voltage of the DC/DC converter in the RPI chassis. For the lower frequencies, the low radiation resistance and high capacitive reactance of the «short» dipole antenna make it virtually impossible to radiate 10 W, especially since the antenna feed voltage was limited to 3000 V_{rms}. Because of the voltage limit, the radiated power reduces from 10 W for $f >$ 260 kHz to ~1mW at 12 kHz. These low power levels require receivers with high sensitivity and large dynamic range as discussed in the feasibility paper by Calvert et al. (1995). Pulse compression and spectral integration techniques, similar to those used in the DPS, provide digital processing gains of nominally 20 dB. Different waveforms, as summarized in Table II are used to adapt the sounding to the diverse conditions in the magnetosphere. Their processing gains are listed in Table III.

To «image» the different plasma regions in the magnetosphere requires the measurement of the arrival angles of the different echoes. The arrival angles can be obtained from the inphase and quadrature samples of the signals from three orthogonal antennas (Reinisch et al., 1999). A single point measurement of the arrival angle with three orthogonal antennas on the ground is more difficult to carry out because of the ground effects, but it can in principle be done (Afraimowich et al., 1999; Morgan and Evans, 1951). The normal of the polarization plane $x' - y'$ (Figure 2) is given by the vector product of two vectors in the polarization plane. Reinisch et al. (1999) suggested the use of the inphase and quadrature field vectors, $\mathbf{E}_i \, x \, \mathbf{E}_q$, that are measured on the three orthogonal antennas at $\omega t = 0$ and $\omega t = \pi/2$ (Calvert, 1999). From the amplitude and phase measurements on the three receive antennas, one can also calculate the wave polarization of the arriving signal if the orientation of the geomagnetic field at the location of the spacecraft is known (Reinisch et al., 1999).

At the time of this writing, some preliminary RPI data have been obtained with the antennas only partially deployed. The plasmagram in Figure 9, showing echo amplitudes as function of virtual range in earth radii R_E versus frequency in kHz, was recorded when IMAGE was in the polar cap at about 5 R_E

Table II. RPI waveforms

Mnemonic	*Description*
SHORT	Simple rectangular pulse of 3.2 ms pulsewidth which defines RPI's range resolution as 480 km (reciprocal of the 300 Hz receiver bandwidth)
COMP4 (or 8, or 16)	4, 8 or 16 chip complimentary phase coded pulses with chip lengths of 3.2 ms.
CHIRP	FM chirp pulse provides high-gain pulse compression with single pulse. Can be repeated for spectral integration.
PLS125 (or 500)	125 or 500 ms long pulse that provides a survey of Doppler shifts at the expense of range resolution.
SPS	Staggered pulse sequence, which consists of 212 pseudo-randomly spaced 3.2 ms pulses at each frequency to provide a maximum number of echoes within the limited coherence time of the medium.

Table III. *Processing gains for different waveforms*

Waveform	*Pulse Compression*	*Spectral Integration*	*Process Gain [dB]*	*Max. Velocity km/sec @ 30 kHz*	*Range Coverage [R_E]*
SHORT	No	Yes	9	5	0.1-10
COMP16[1]	Yes	Yes	21	5	1.2-10
CHIRP	Yes	No[2]	18	750[3]	2.4-8
PLS125	No	Yes	20	750[3]	1.5-10
SPS	No	Yes	21	750[3]	0.1-19

[1] assuming 8 pulse repetitions at 2 Hz rate
[2] Doppler integration can also be obtained by repeating chirp pulse N times
[3] 300 Hz receiver bandwidth sets velocity limit

altitude The two echo traces seen between 60 and 160 kHz come from the day-side and nightside plasmasphere. When operating in the receive-only mode, RPI acts as a spectrometer measuring the field strength of electromagnetic emissions and thermal noise (Meyer-Vernet and Perche, 1989). Figure 10 shows the dynamic spectrogram with noise amplitude plotted as function of frequency and time of day for May. The sequence of 10-minute noise measurements was interlaced with echo sounding measurements of the type shown in

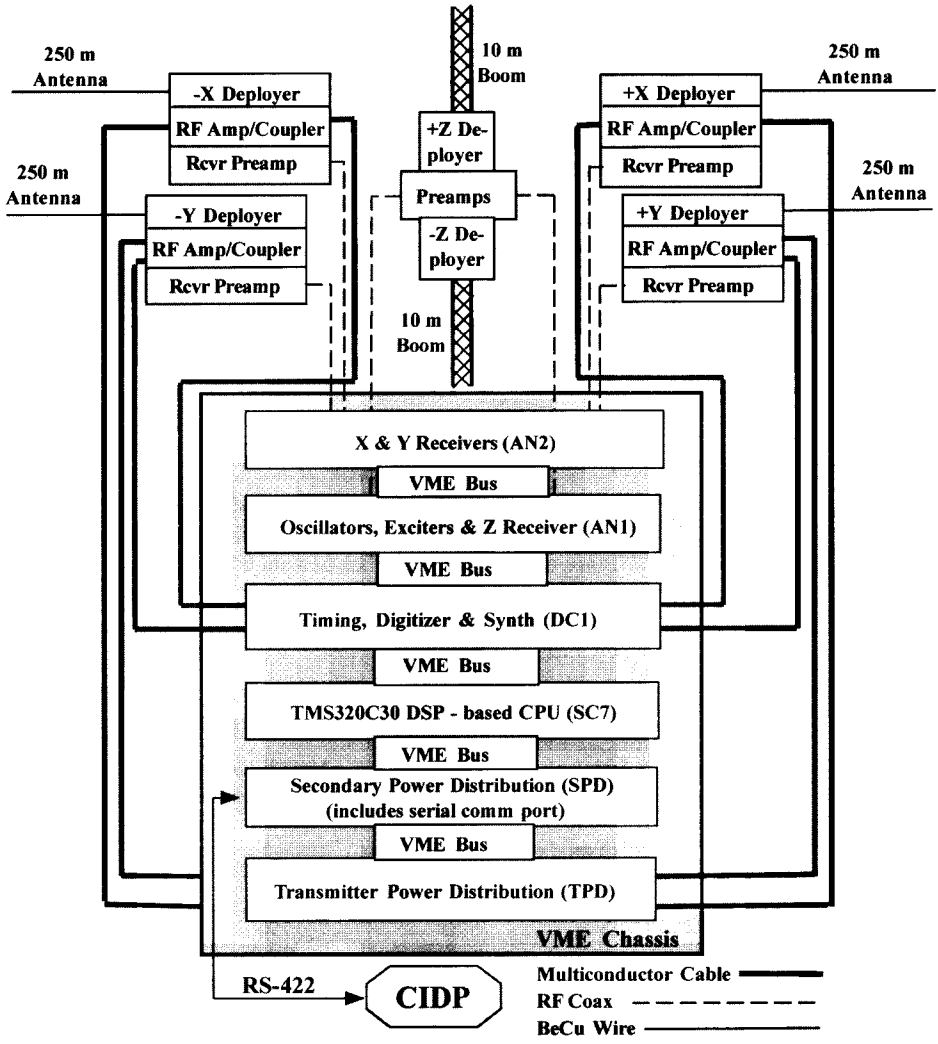

Figure 7. RPI block diagram. RPI data and controls are handled by the common instrument data processor (CIDP) (Gibson et al., 2000).

Figure 9. The local plasma frequency f_{NS}, shown as a noise enhancement, varies from below 10 kHz in the magnetospheric cavity to ~200 kHz near perigee (1000 km altitude). Electromagnetic emissions are received for $f > f_{NS}$; type III radio bursts are seen at the upper frequencies between 11 and 14 UT. These high-resolution spectrograms will offer important inputs for space weather studies.

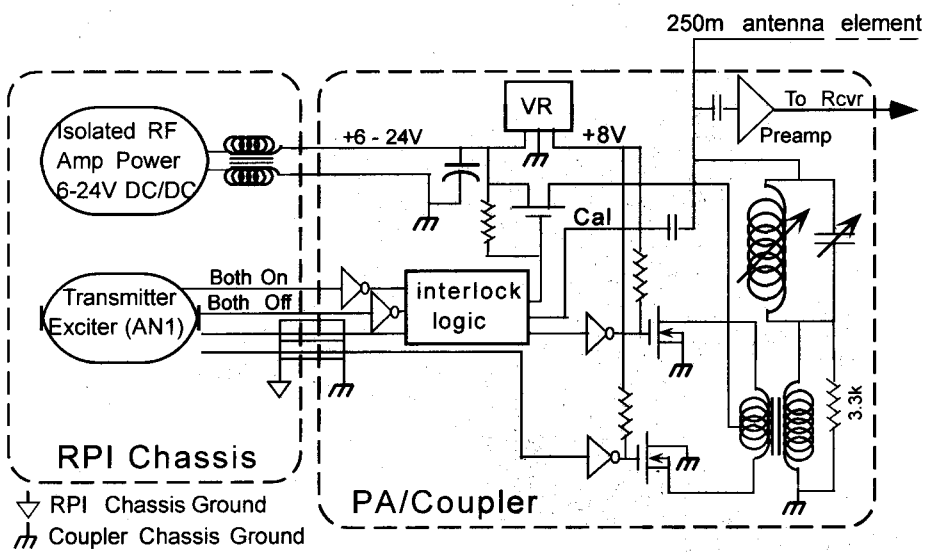

(a)

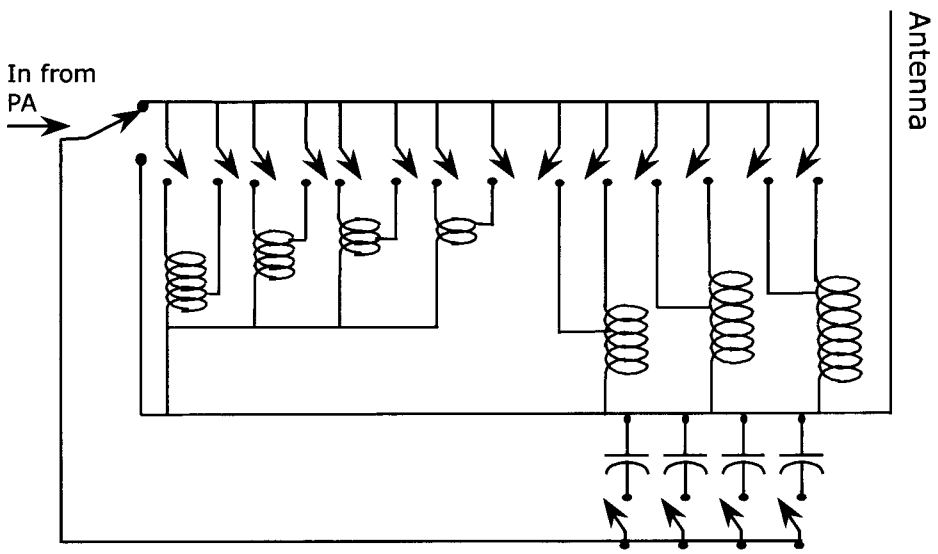

(b)

Figure 8. RPI power amplifier and coupler

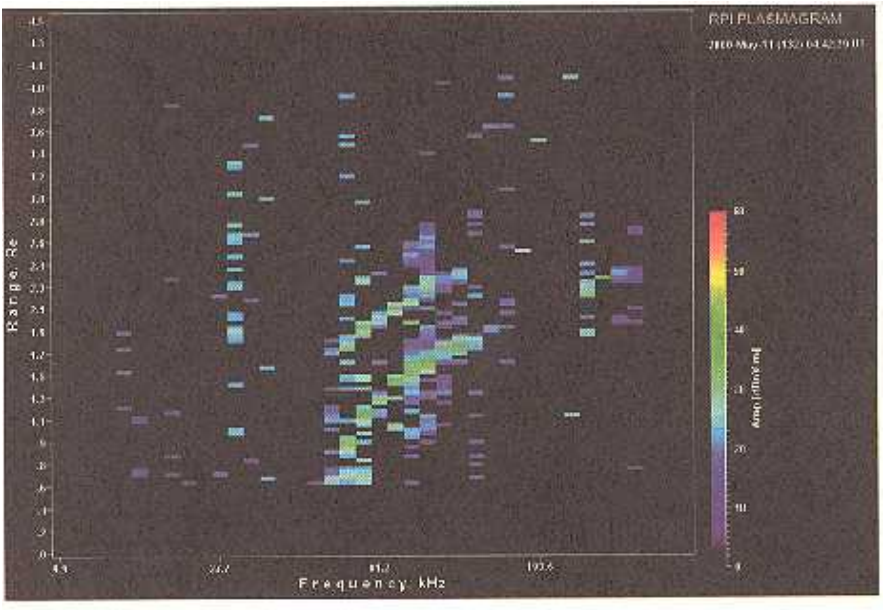

Figure 9. Early RPI plasmagram with simultaneous echo traces from the dayside and nightside plasmasphere. IMAGE was at an altitude of 3.8 R_E.

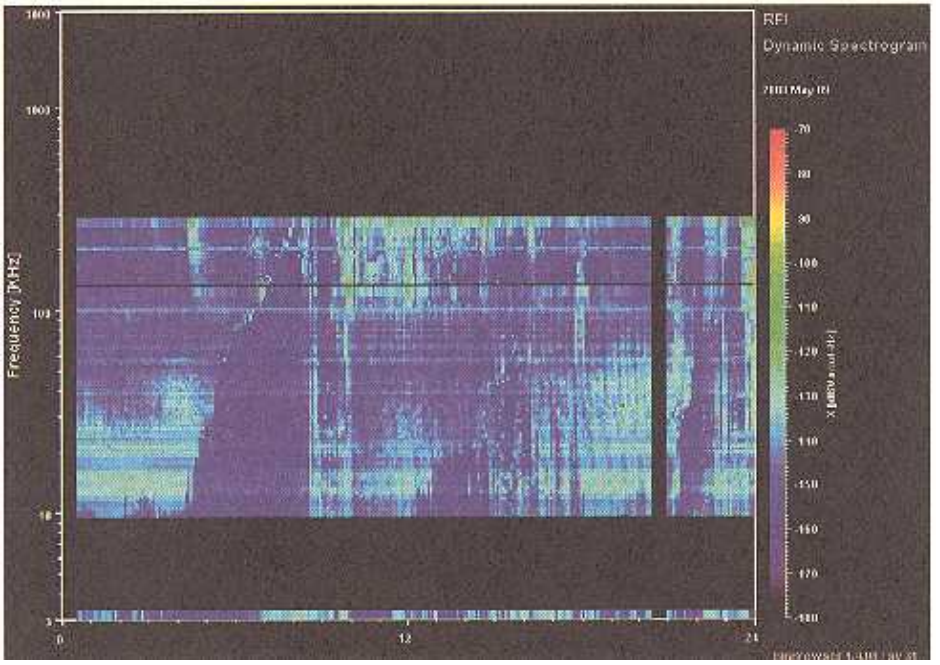

Figure 10. Dynamic spectrogram showing thermal noise signals and electromagnetic emissions in the frequency range from 3 - 280 kHz for 09 May 2000.

7. SUMMARY

Modern geospace plasma sounders are extremely versatile tools for ground-based and space-borne observations. Their potential for the exploration of the plasma universe is just beginning to evolve. The important breakthrough was the development of Doppler-sorted imaging with antennas that are usually small compared to the wavelength of the sounder frequencies. This makes it possible to measure the structure and dynamics of geospace plasmas. Use of coherent spread-spectrum waveforms and digital processing techniques has reduced the requirements for the transmitter power by several orders of magnitude compared to older systems, reducing RF pollution as well system costs. The next important task is to apply the advanced sounding techniques to topside ionospheric sounding from satellites at nominal altitudes of 1000 to 2000 km to map the plasma region between the peak of the F2 layer and the plasmasphere, which is only poorly known. Automatic techniques for the scaling of topside ionograms and the calculation of the topside profiles, previously developed by Huang and Reinisch (1982), could supply real time information in support of space weather applications once a topside sounder with Doppler imaging capability is in orbit.

8. REFERENCES

AFRAIMOVITCH, E. L.; CHERNUKHOV, V. V.; KOBZAR, V. A., and PALAMARTCHOUK, K. S. (1999): «Determining polarization parameters and angles of arrival of HF radio signals using three mutually orthogonal antennas», *Radio Sci.*, 34, 5, 1217-1225.

BARRY, G. H. (1971): «A low-power vertical-incidence ionosonde», *IEEE Trans.*, GE-9, 86-95.

BENSON, R. F.; REINISCH, B.W.; GREEN, J. L.; FUNG, S. F.; CALVERT, W.; HAINES, D. M.; BOUGERET, J. L.; MANNING, R.; CARPENTER, D. L.; GALLAGHER, D. L.; REIFF, P. H., and TAYLOR, W. W. L. (1998): «Magnetospheric radio sounding on the IMAGE mission», *Radio Science Bulletin*, No. 285, ISSN 1024-4530, International Union of Radio Science, URSI, c/o University of Gent, 9-20.

BIBL, K., and REINISCH, B.W. (1978): «The universal digital ionosonde», *Radio Sci.*, 13, 519-530.

BOUGERET, J. L.; KAISER, M.L.; KELLOGG, P. G.; MANNING, R.; GOETZ, K.; MONSON, S. J.; MONGE, N.; FRIEL, L.; MEETRE, C. A.; PERCHE, V.; CITRUIK, L., and HOANG, S. (1995): «Waves; the radio plasma wave investigation on the WIND spacecraft», *Space Sci. Rev.*, 71, 231-263.

BREIT, G., and TUVE, M. A. (1926): «A test for the existence of the conducting layer», *Phys. Rev.*, 28, 554-575.

BUDDEN, K. G. (1985): *The propagation of radio waves, the theory of radio waves of low power in the ionosphere and magnetosphere*, Cambridge University Press, New York, 669 pp.

BURCH, J. L. (2000): «IMAGE mission overview», *Space Sci. Rev.*, 91, 1-14.

CALVERT, W.; BENSON, R. F.; CARPENTER, D. L.; FUNG, S. F.; GALLAGHER, D. L.; GREEN, J. L.; HAINES, D. M.; REIFF, P. H.; REINISCH, B. W.; SMITH, M. F., and TAYLOR, W. W. L. (1995): «The feasibility of radio sounding in the magnetosphere», *Radio Sci.*, 30, 1577-1595.

CALVERT, W. (1999): «Method for measuring the direction and wave mode of the radio echoes that are detected by a satellite radio sounder in the Earth's magnetosphere». *Radio Sci.*, 34, 5, 1287-1297.

CANNON, P. S.; REINISCH, B. W.; BUCHAU, J., and BULLETT, T. W. (1991): «Response of the Polar Cap F Region Convection Direction to Changes in the Interplanetary Magnetic Field: Digisonde Measurements in Northern Greenland», *J. Geophys. Res.*, 96, A2, 1239-1250.

FRANKLIN, C. A., and MACLEAN, M. A. (1969): «The design of swept-frequency topside sounders», *Proc. IEEE*, 57, 897-929.

FUSILIER, S. A.; BURCH, J. L.; LEWIS, W. S., and REIFF, P. H. (2000): «Overview of the IMAGE science objectives and mission phases», *Space Sci. Rev.*, 91, 51-66.

GRUBB, R. N. (1979): «The SEL HF Radar Systems (Ionospheric Sounders)», *NOAA Tech. Memo.* ERL SEL-55, Boulder CO, USA.

GURNETT, D. A., et al. (1995): «The polar plasma wave instrument», *Space Sci. Rev.*, 71, 597-622.

HAINES, D. M. (1994): «A portable ionosonde using coherent spread-spectrum waveforms for remote sensing of the ionosphere», *Thesis, University of Massachusetts Lowell.*

HUANG, X., and REINISCH, B. W. (1982): «Automatic calculation of electron density profiles from digital ionograms 2. True height inversion of topside ionograms with the profile-fitting method», *Radio Sci.*, 17, 837-844.

HUNSUCKER, R. D. (1992): *Radio Techniques for Probing the Terrestrial Ionosphere*, Vol. 22, Phys. Chem. Space, Springer-Verlag, Berlin.

JACKSON, J. E. (1986): «Alouette-ISIS Program Summary», *NSSDC Report 86-09*, National Space Science Data Center, Greenbelt, MD.

JACKSON, J. E.; SCHMERLING, E. R., and WHITTEKER, J. H. (1980): «Mini-review on topside sounding», *IEEE Trans. Antennas Propagat.*, AP-28, 284-288.

MEYER-VERNET, N., and PERCHE, C. (1989): «Toolkit for antennae and thermal noise near the plasma frequency», *J. Geophys. Res.*, 94, 2405-24014.

MORGAN, M., and EVANS, W. (1951): «Synthesis and analysis of elliptic polarization loci in terms of space-quadrature sinusoidal components», *Proc. IRE*, 39, 552-556.

MCDOUGAL, J. W.; GRANT, I. F., and SHEN, X. (1995): «The Canadian digital ionosonde: design and results», *WDC-A for Solar-Terrestrial Physics*, UAG-104, Ionosonde Networks and Stations, 21-27.

PULINETS, S. A. (1989): *Prospects of topside sounding, in WITS Handbook No. 2*, edited by C.H. Liu, SCOSTEP Publishing, Urbana, IL, 99-127.

RAWER, K., and SUCHY, K. (1967): «Radio Observations of the Ionosphere», in S. Flügge (ed.), *Encyclopedia of Physics*, XLIX/2, Geophysics III/2, Sect. 7, Springer-Verlag, Berlin.

REINISCH, B. W., and HUANG, X. (1983): «Automatic Calculation of Electron Density Profiles from Digital Ionograms, 3. Processing of bottomside ionograms», *Radio Sci.*, 18 (3), 477-492.

REINISCH, B. W.; BUCHAU, J., and WEBER, E. J. (1987): «Digital Ionosonde Observations of the Polar Cap F Region Convection», *Physica. Scripta.*, 36, 372-377.

REINISCH, B. W.; BIBL, K.; KITROSSER, D. F.; SALES, G. S.; TANG, J. S.; ZHANG, Z. M.; BULLETT, T. W., and RALLS, J. A. (1989): *The Digisonde 256 ionospheric sounder*, World Ionosphere/Thermosphere Study, WITS Handbook, Vol. 2, C.H. Liu (Ed.), 350-382.

REINISCH, B. W.; HAINES, D. M.; BIBL, K.; GALKIN, I.; HUANG, X.; KITROSSER, D. F.; SALES, G. S., and SCALI, J. L. (1997): «Ionospheric sounding in support of over-the-horizon radar», *Radio Sci.*, 32 (4), 1681-1694.

REINISCH, B.W. (1996): *Modern Ionosondes*, in Modern Ionospheric Science, edited by H. Kohl, R. Rüster and K. Schlegel, European Geophysical Society, Katlenburg-Lindau, Germany, 440-458.

REINISCH, B.W.; SALES, G. S.; HAINES, D. M.; FUNG, S. F., and TAYLOR, W.W.L. (1999): «Radio wave active Doppler imaging of space plasma structures: angle-of-arrival, wave polarization, and Faraday rotation measurements with RPI», *Radio Sci.*, 34 (6), 1513-1524.

REINISCH, B.W.; HAINES, D.M.; BIBL, K.; CHENEY, G.; GALKIN, I. A.; HUANG, X.; MYERS, S. H.; SALES, G. S.; BENSON, R. F.; FUNG, S. F.; GREEN, J. L.; BOARDSEN, S.; TAYLOR, W. W. L.; BOUGERET, J. L.; MANNING, R.; MEYER-VERNET, N.; MONCUQUET, M.; CARPENTER, D. L.; GALLAGHER, D. L., and REIFF, P. H. (2000): «The Radio Plasma Imager investigation on the IMAGE spacecraft», *Space Science Reviews*, 91, 319-359.

REZNIKOV, A. E. (1991): «A new ionosonde», *INAG Bulletin*, 56, 3-4.

SALES, G. S.; REINISCH, B. W.; SCALI, J. L.; DOZOIS, C.; BULLETT, T. W.; WEBER, E. J., and NING, P.: «Spread-F and the structure of equatorial ionization depletions in the Southern Anomaly Region», J. Geophys. Res., Vol. 101, No. A12, pp. 26,819-26,827, 1996.

SCALI, J. L.; REINISCH, B.W.; HEINSELMAN, and BULLETT, T. W. (1995): «Coordinated Digisonde and incoherent scatter radar F region drift measurements at Sondre Stromfjord», *Radio Sci.*, 30, 1481-1498.

SMITH, P. R.; DYSON, P. L.; MONSELESAN, D. P., and MORRIS, R. J. (1998): «Ionospheric convection at Casey, a southern polar cap station», *J. Geophys. Res.*, 103, 2209-2218.

STIX, T. H. (1992): *The Theory of Plasma Waves*, McGraw-Hill, New York, 1962.

WRIGHT, J. W., and PITTEWAY, M. L. V. (1979): «Real time data acquisition and interpretation capabilities of the Dynasonde», *Radio Sci.*, 14, 815-835.